

Narrow-band spectral analysis and thin-bed tuning

K. J. Marfurt* and R. L. Kirlin[†]

ABSTRACT

Running window seismic spectral decomposition has proven to be a very powerful tool in analyzing difficult-to-delineate thin-bed tuning effects associated with variable-thickness sand channels, fans, and bars along an interpreted seismic horizon or time slice. Unfortunately, direct application of spectral decomposition to a large 3-D data set can result in a rather unwieldy 4-D cube of data. We develop a suite of new seismic attributes that reduces the input 20–60 running window spectral components down to a workable subset that allows us to quickly map thin-bed tuning effects in three dimensions.

We demonstrate the effectiveness of these new attributes by applying them to a large spec survey from the Gulf of Mexico. These two thin-bed seismic attributes provide a fast, economic tool that, when coupled with other attributes such as seismic coherence and when interpreted within the framework of geomorphology and sequence stratigraphy, can help us quickly evaluate large 3-D seismic surveys. Ironically, in addition to being more quantitatively linked to bed thickness, the thin-bed attributes described here allow us to analyze thicker features than the conventional instantaneous and response frequencies, which cannot calculate the spectral interference between two well-separated reflectors.

INTRODUCTION

During the past two decades, advances in velocity analysis and seismic migration algorithms have greatly improved our ability to image large-scale complex structures. During the same period, our ability to image small-scale structures internal to petroleum reservoirs has improved only moderately. Internal structures and even the reservoirs themselves are at or below seismic resolution and exhibit themselves as subtle variations in amplitude and phase rather than as changes in event arrival time. One of our major challenges as an industry is to

take these poorly resolved images and improve our estimates of net-to-gross volume, lithology, and fluid type that define our reservoir models.

Clearly, one of the most fundamental reservoir characteristics is thickness. The analysis of thin-bed tuning on seismic reflectivity has been studied extensively by Widess (1973) and Neidel and Poggiagliomi (1977), who discuss the limits of seismic resolution. Robertson and Nogami (1984) show how Taner et al.'s (1979) instantaneous attributes can be used to map thin beds. Bodine (1986) modifies Taner et al.'s (1979) original instantaneous attributes to obtain response attributes that more closely reflect the characteristics of the reflected wavelet as a whole. Bahorich and Bridges (1992) show how these attributes can be extracted along interpreted horizons to allow direct mapping of bright spots, dim spots, and, in general, lithologic packages. During the past decade, our industry has developed a plethora of new attributes, including dip/azimuth (Dalley et al., 1989; Luo et al., 1996; Marfurt et al., 1998), coherence (Bahorich and Farmer, 1995; Marfurt et al., 1998; Gersztenkorn and Marfurt, 1999) lateral variation of amplitude (Marfurt and Kirlin, 2000), spectral decomposition (Peyton et al., 1998; Partyka et al., 1999), and amplitude versus bandwidth (Kelley et al., 1992). Radovich and Oliveros (1998), Hesthammer and Fossen (1997), and Hesthammer (1998) summarize how these attributes can be applied to seismic interpretation.

No geophysicist can expect to interpret more than a few seismic attributes at a time for even a single horizon, let alone multiple horizons within a 3-D volume. To this end the seismic industry is investing considerable effort in developing multiattribute analysis techniques, including multiattribute 3-D visualization, principal component analysis, cluster analysis, feature extraction, and neural nets. The goal of much of this work is to be able to handle up to a dozen or more attribute maps, to determine which (or which combinations of) attributes are most closely linked to reservoir parameters of interest, and then to convert our input attribute maps into a probabilistic map of reservoir parameters. The most aggressive application of such sophisticated analysis would be to use the raw seismic time samples themselves, which just happens to be the method of

Manuscript received by the Editor January 27, 1999; revised manuscript received August 8, 2000.

*University of Houston, Department of Geosciences, Allied Geophysics Laboratories, 4800 Calhoun Road, Houston, Texas 7204-5505. E-mail: kmarfurt@uh.edu.

[†]University of Victoria, ECE Department, Victoria, British Columbia V8W3P6, Canada. E-mail: kirlin@enr.uvic.ca.

© 2001 Society of Exploration Geophysicists. All rights reserved.

choice for one of the more popular software developers on the market. Alternatively, the interpreter could analyze the complete amplitude and phase spectra within a temporal analysis window. We feel it is prudent to select or develop a few attributes that are tightly linked to the geology and physics of the problem we wish to map, be they related to the presence of hydro-carbons, structural edges, or stratigraphic textures. For this very reason, one of the most important attributes today is simple amplitude extraction for bright-spot analysis, since it is directly related to the presence of gas.

In this paper we focus exclusively on thin-bed attribute analysis. We begin by reviewing the simple theory of thin-bed tuning and instantaneous attributes. We then build on the foundation laid by Partyka et al. (1999) and Okaya (1995) to develop a suite of single trace attributes that are more closely related to the theoretical tuning thickness. Next, we extend Partyka et al.'s (1999) algorithm to analyze narrow-band lateral variations in reflectivity, giving rise to an additional suite of seismic texture attributes. Finally, we calibrate these attributes by applying them to a test data set and a corresponding synthetic data set collected over a sand-filled channel embedded in a shale matrix offshore Gulf of Mexico. We conclude our study by showing how some of these attributes can be used in the quick evaluation of a large spec survey.

The thin-bed response

We begin our analysis by defining the reflection impulse response from the thin bed shown in Figure 1. The time-domain impulse response, or Green's function, $g(t)$ is given by

$$g(t, \theta) = r_1 \delta(t - t_1) + r_2 \delta[t - t_1 - T], \quad (1)$$

where r_1 = the angle-dependent reflection coefficient from the top of the thin bed, r_2 = the angle-dependent reflection coefficient from the bottom of the thin bed, t_1 = the two-way traveltime to the top of the thin bed, t_2 = the two-way traveltime to the bottom of the thin bed, $T = t_2 - t_1$ = the two-way traveltime thickness of the thin bed, and $\delta(t)$ = the Dirac δ function. (A nomenclature list is provided in Table 1.)

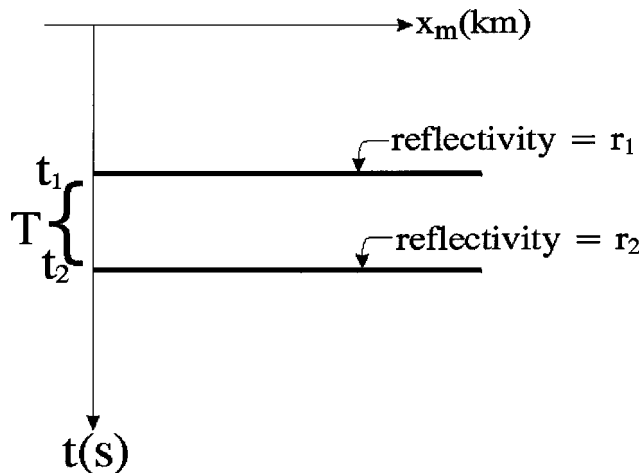


FIG. 1. The thin-bed model. The top of the thin bed is at time t_1 with reflectivity $r_1(\theta)$. The bottom of the thin bed is at time t_2 with reflectivity $r_2(\theta)$. The bed thickness is $T(\theta) = t_2 - t_1(\theta)$.

The frequency-domain impulse response, or Green's function, $G(f)$ is given by

$$G(f) = r_1(\theta) \exp(-i2\pi f t_1) + r_2(\theta) \exp\{-i2\pi f [t_1 + T]\}, \quad (2)$$

where f is the temporal frequency measured in hertz. We plot the amplitude of $G(f)$ in Figure 2a for the case $r_1/r_2 < 0$ and note that the spectral minima occur at frequencies $f = (n + 1/2)/T$, while the spectral maxima occur at frequencies $f = n/T$. In Figure 2b, we plot the magnitude of $G(f)$ when $r_1/r_2 > 0$. In this case the spectral maxima occur at frequencies $f = (n + 1/2)/T$, while the spectral minima occur at $f = n/T$. This case of r_1 and r_2 having opposite signs commonly occurs for thin sand channels embedded in a shale matrix. Since we can more robustly pick maxima than minima, it is fortuitous

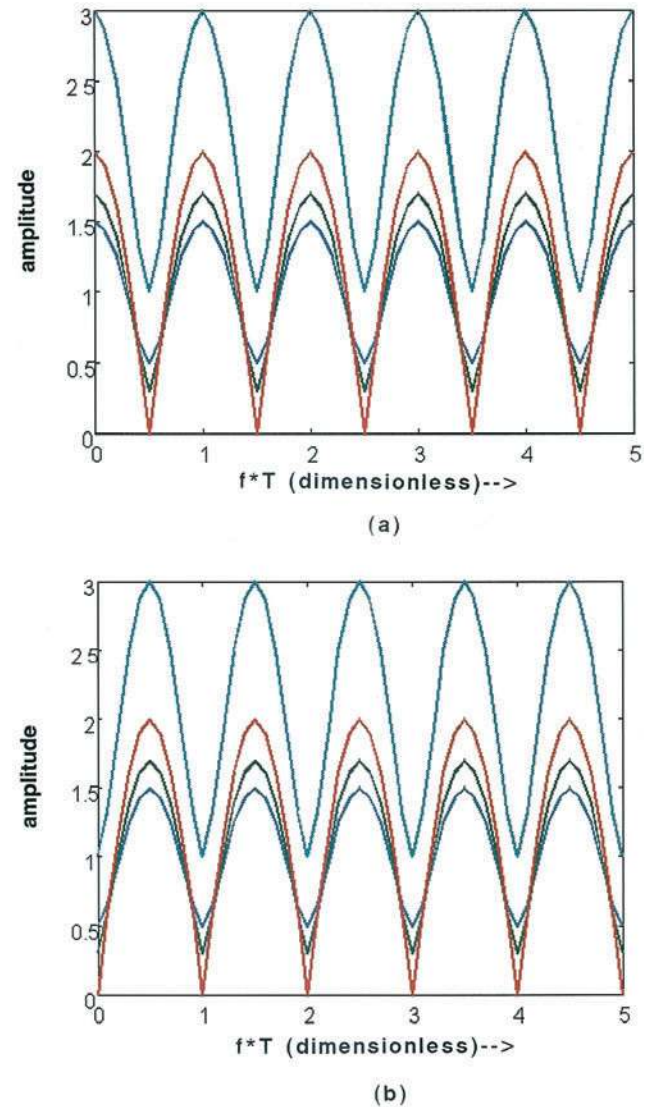


FIG. 2. The amplitude of the thin-bed reflection as a function of frequency f for (a) $r_1/r_2 = -2.0$ (cyan), -1.0 (red), -0.7 (green), -0.5 (blue), and (b) $r_1/r_2 = +2.0$ (cyan), $+1.0$ (red), $+0.7$ (green), $+0.5$ (blue).

that the first spectral peak occurs at $f = 1/2T$, increasing the chance that it will fall within the seismic recording frequency band.

We will also find it useful to examine the change in phase $\phi(f, T)$ with frequency f ,

$$\frac{\partial \phi(f, T)}{\partial f} = -2\pi T \frac{r_1 r_2 \cos(2\pi f T) + r_2^2}{2r_1 r_2 \cos(2\pi f T) + r_1^2 + r_2^2}, \quad (3)$$

and with thickness T ,

$$\frac{\partial \phi(f, T)}{\partial T} = -2\pi f \frac{r_1 r_2 \cos(2\pi f T) + r_2^2}{2r_1 r_2 \cos(2\pi f T) + r_1^2 + r_2^2}. \quad (4)$$

Table 1. Nomenclature.

$d_j(t)$	= seismic data at trace j and time t
$h_j(t)$	= Hilbert transform, or quadrature of the seismic data $d_j(t)$
$z_j(t)$	= $d_j(t) + ih_j(t)$, analytic trace corresponding to $d_j(t)$
$e_j(t)$	= instantaneous envelope of the analytic trace $z_j(t)$
$\psi_j(t)$	= instantaneous phase of the analytic trace $z_j(t)$
$f_j^{\text{inst}}(t)$	= instantaneous frequency of the analytic trace $z_j(t)$
$w_j(f, t)$	= short-window Fourier transform of $d_j(t)$ at frequency f centered about time t .
$u_j(f, t)$	= real part of $w_j(f, t)$
$v_j(f, t)$	= imaginary part of $w_j(f, t)$
$a_j(f, t)$	= amplitude or magnitude of $w_j(f, t)$
$\phi_j(f, t)$	= phase of $w_j(f, t)$
$c(f, t)$	= tapered cosine wavelet transform operator
$s(f, t)$	= tapered sine wavelet transform operator
$m(t)$	= tapered window used in constructing $c(f, t)$ and $s(f, t)$
$E^p(f, t)$	= L - p norm of $w_j(f, t)$ over all traces j for fixed time slice t and frequency f .
f_{\min}, f_{\max}	= minimum and maximum frequencies to be analyzed, in hertz
Δf	= spectral sampling interval, in hertz
Δt	= temporal sampling interval, in hertz
$f^{\text{peak}}(t)$	= frequency at which the amplitude spectrum $a_j(f, t)$ is maximum
$f^{\text{trough}}(t)$	= frequency at which the amplitude spectrum $a_j(f, t)$ is minimum
$a_j^{\text{peak}}(t)$	= $a_j(f^{\text{peak}}, t)$ = maximum amplitude of the amplitude spectrum $a_j(f, t)$
$a_j^{\text{trough}}(t)$	= $a_j(f^{\text{trough}}, t)$ = minimum amplitude of the amplitude spectrum $a_j(f, t)$
$R_j(t)$	= $a_j^{\text{trough}}(t)/a_j^{\text{peak}}(t)$ = spectral amplitude ratio
$g(t)$	= time-domain impulse response from a thin bed for a plane wave incident at angle θ at time t
r_1	= angle-dependent reflection coefficient from the top of the thin bed
r_2	= angle-dependent reflection coefficient from the bottom of the thin bed
t_1	= two-way traveltime to the top of the thin bed
t_2	= two-way traveltime to the bottom of the thin bed
$T = t_2 - t_1$	= two-way travel thickness of the thin bed
$\delta(t)$	= Dirac δ function
$G(f)$	= frequency-domain impulse response from a thin bed for a plane wave incident at angle θ at frequency f

Equations (3) and (4) have a minimum (for $0 < r_1/r_2 < 1$) when $fT = 2\pi n$ and a maximum when $fT = 2\pi(n+1/2)$ where n is an integer. We display these results for a fixed value of $T = 50$ ms in Figure 3a, noting that the peak of $\partial\phi/\partial f$ becomes sharper as the ratio r_1/r_2 approaches $+1$ or -1 , where equations (3) and (4) degenerate to constant values of $\partial\phi/\partial f$ and $\partial\phi/\partial T$. For values of $|r_1/r_2|$ not equal to unity, we note that for a fixed value of f the peaks in $\partial\phi/\partial f$ form contours in constant thickness T . We show the behavior of $\partial\phi/\partial f$ as a function of f and T in Figures 3b and 3c. We will examine the use of such contours on synthetic and real data later in this paper.

We now examine a cross-section through a sand-filled (thin-bed) channel from the Gulf of Mexico shown in Figures 4a and 4b. In Figure 4c we extract the amplitude along the horizon that forms the top of the channel. To better calibrate our seismic attributes, we next generate a synthetic seismic section corresponding to two picked horizons defining the top and bottom of the channel, where we have assumed $r_1/r_2 = -0.9$, and display the results in Figure 5.

Finally, we display the two-way traveltime thickness T in Figure 6a and the theoretical peak frequency $f^{\text{peak}} = 1/2T$ in Figure 6b.

Broadband single-trace spectral attributes

Taner et al. (1979) applied analytic (often called complex) trace analysis to seismic data two decades ago, giving rise to a family of seismic attributes that are still widely used by seismic interpreters. We will focus on three attributes: the instantaneous envelope, phase, and frequency. Given seismic data $d_j(t)$ for trace j at time t , we define the analytic trace $z_j(t)$ to be

$$z_j(t) = d_j(t) + ih_j(t), \quad (5)$$

where $h_j(t)$ is the Hilbert transform (also called the quadrature) of $d_j(t)$ and $i = (-1)^{1/2}$. We follow Taner et al. (1979) and define the instantaneous envelope $e_j(t)$,

$$e_j(t) = [d_j^2(t) + h_j^2(t)]^{1/2}, \quad (6)$$

the instantaneous phase $\psi(t)$,

$$\psi_j(t) = \tan^{-1} \left[\frac{h_j(t)}{d_j(t)} \right], \quad (7)$$

and the instantaneous frequency $f_j^{\text{inst}}(t)$,

$$\begin{aligned} f_j^{\text{inst}}(t) &= \frac{d}{dt} \psi_j(t) = \frac{d}{dt} \tan^{-1} \left[\frac{h_j(t)}{d_j(t)} \right] \\ &= \frac{d_j(t) \frac{d}{dt} h_j(t) - h_j(t) \frac{d}{dt} d_j(t)}{e_j(t)^2}. \end{aligned} \quad (8)$$

By defining $f_j^{\text{inst}}(t)$ in equation (6) as the derivative of $\tan^{-1}[h_j(t)/d_j(t)]$, Taner et al. (1979) avoided the need to unwrap the phase $\psi(t)$. Bodine (1986) defines the response attributes to be the instantaneous attributes measured at the peak of the envelope lobe within which the seismic analysis point falls.

We calculate the response envelope $e_j(t)$ and response frequency $f_j(t)$ for the synthetic shown in Figure 5 and display

the results in Figures 7, noting reasonably good correlation between the picked channel thickness shown in Figure 6a and the response frequency shown in Figure 7b. However, even though they are correlated, the response frequency displayed in Figure 7b is not equal to the predicted peak frequencies displayed in Figure 6b.

Narrow-band single-trace spectral attributes

We follow Partyka et al. (1999) and decompose a $2N + 1$ sample-length window of seismic data $d_j(t + n\Delta t)$, where $(-N \leq n \leq +N)$, into its Fourier components $w(f, t)$:

$$w(f, t) = u(f, t) + i v(f, t), \quad (9)$$

where

$$u(f, t) = \sum_{n=-N}^{+N} c(f, n\Delta t) d(t + n\Delta t), \quad (10)$$

$$v(f, t) = \sum_{n=-N}^{+N} s(f, n\Delta t) d(t + n\Delta t), \quad (11)$$

$$c(f, t) = m(t) \cos(2\pi f t), \quad (12)$$

$$s(f, t) = m(t) \sin(2\pi f t), \quad (13)$$

and $m(t)$ is a window having fixed-length Tukey (raised cosine) tapers at each end. The spectrum of $c(f, t)$ and $s(f, t)$ forms a narrow band centered about frequency f , with the width determined by the size and tapers of the temporal analysis window $m(t)$. Applying a longer window results in increased spectral resolution but decreased temporal resolution. Longer tapers decrease spectral resolution but also decrease spectral ambiguity because of side lobes. We must of course take care not to analyze low frequencies whose periods $T = 1/f$ exceed the length of our analysis window. In this situation, the spectrum of the analysis wavelets $c(f, t)$ and $s(f, t)$, wrap around below 0 Hz and alias into the high-frequency band, such that we could naively mistake a broadband, high-frequency response for a narrow-band, low-frequency response.

Also following Partyka et al. (1999), we assume that the geology of any time slice is sufficiently complex such that we can

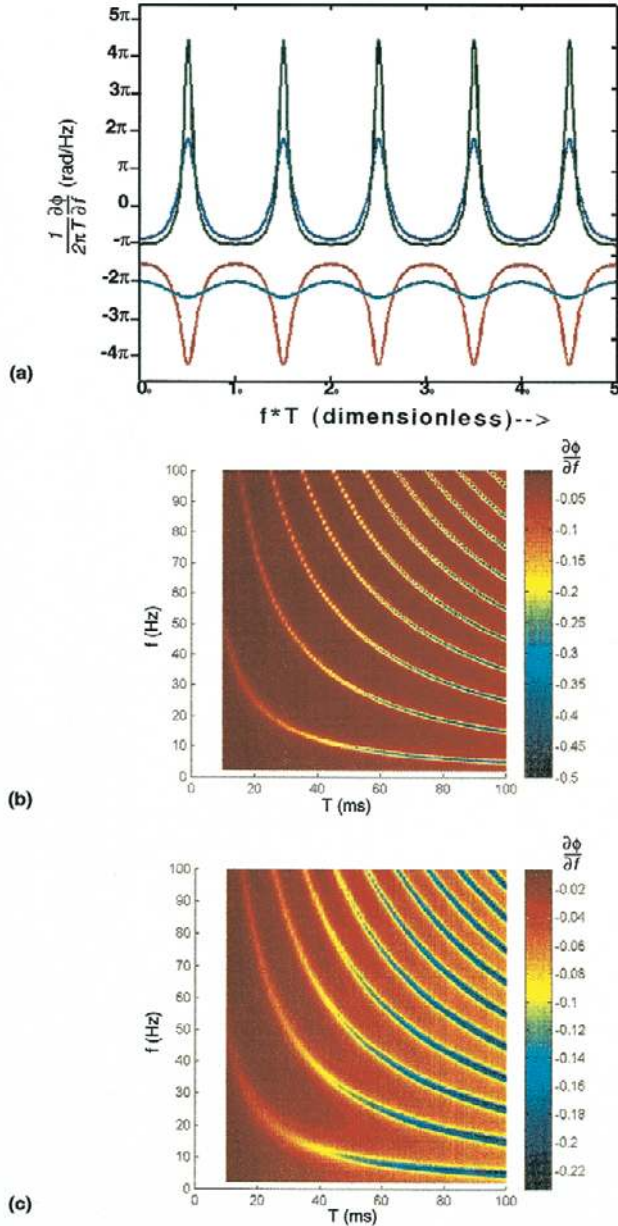


FIG. 3. (a) The rate of change of phase with respect to frequency $d\phi/df$ for the thin-bed reflection as a function of normalized frequency fT for $r_2/r_1 = 0.5, 0.7, 2.0$, and 10.0 . The value $d\phi/df$ is a function of f and T for (b) $r_1/r_2 = 1.25$ and (c) $r_1/r_2 = 1.75$.

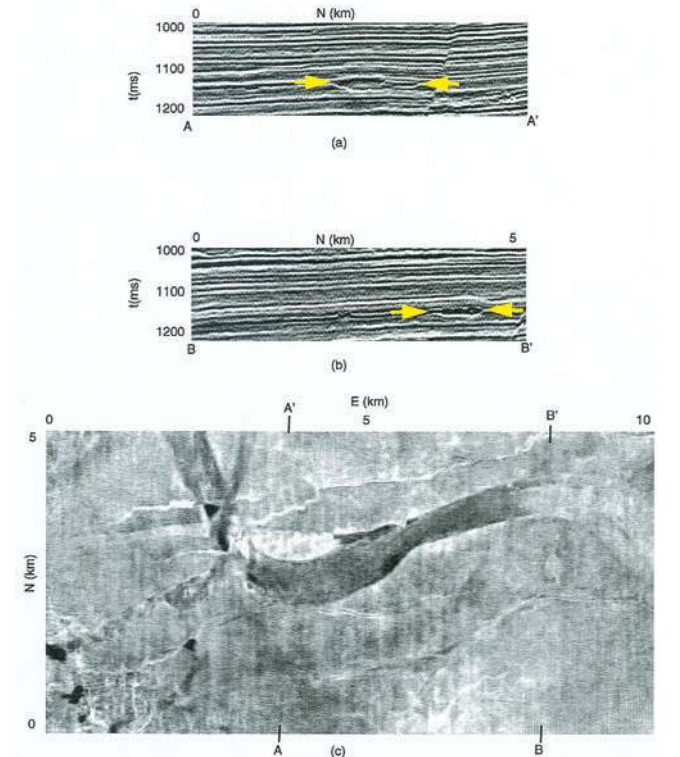


FIG. 4. (a) and (b) Cross-sections of a sand-filled channel enclosed in a shale matrix from the Gulf of Mexico. (c) An amplitude extraction map made along the top of the channel. Black corresponds to a trough, white to a peak.

consider its reflectivity spectrum to be white. We scale our data such that the L - p norm of each (f, t) plane,

$$E^p(f, t) = \left[\sum_{\text{all } j} u_j^p(f, t) + v_j^p(f, t) \right]^{1/p}, \quad (14)$$

has the same value, thereby removing most of the amplitude variation effects of the source wavelet, including attenuation with time.

One of the most useful yet simplest seismic attributes to extract from the spectral decomposition cube is the peak frequency, defined as that frequency f at which the amplitude $a_j(f, t)$ defined by

$$a_j(f, t) = [u_j^2(f, t) + v_j^2(f, t)]^{1/2} \quad (15)$$

is maximum.

Discrete Fourier transform theory only requires that, for an analysis window of length T_a , we sample the frequency at a rate of $\Delta f = 1/T_a$, between f_{\min} and f_{\max} , after which we can accurately interpolate $u_j(f, t)$ and $v_j(f, t)$ for any intermediate frequency. In principle, we could solve for the peak amplitude of equation (15) through differentiation of $a_j(f, t)$ and appropriate application of interpolation operators and the chain rule to $u_j(f, t)$ and $v_j(f, t)$. In practice, it is far simpler to decrease Δf to about twice the required

sampling rate, whereafter we can directly interpolate $a_j(f, t)$. For thick beds we may encounter more than one peak in the amplitude spectrum. We try to avoid this ambiguity by designing our algorithm to pick the peak having the lowest frequency.

We will always find a peak (or trough) frequency in any amplitude spectrum $a_j(f, t)$ we choose to analyze—even for areas of our survey having little geological interest. To differentiate peak (or trough) frequencies corresponding to reservoirs associated with bright spots, we need to extract two additional attributes, the amplitudes at the peak and trough frequencies:

$$a_j^{\text{peak}}(t) = a_j(f^{\text{peak}}, t) \quad (16)$$

and

$$a_j^{\text{trough}}(t) = a_j(f^{\text{trough}}, t). \quad (17)$$

Together, f^{peak} , f^{trough} , a_j^{peak} , and a_j^{trough} capture the essence of the spectrum as a result of thin-bed tuning. Since the theoretical thin-bed amplitude response is minimum at $f^{\text{trough}}(t)$, we expect the estimate of a_j^{trough} to be dominated by noise. This poor estimate in turn will hamper our ability to estimate $f^{\text{trough}}(t)$ accurately. We display $f^{\text{peak}}(t)$ and $f^{\text{trough}}(t)$ for the real data set corresponding to Figure 4 in Figures 8a and 8b. We display $a_j(f^{\text{peak}}, t)$ and $a_j(f^{\text{trough}}, t)$ in Figures 9a and 9b. Within the

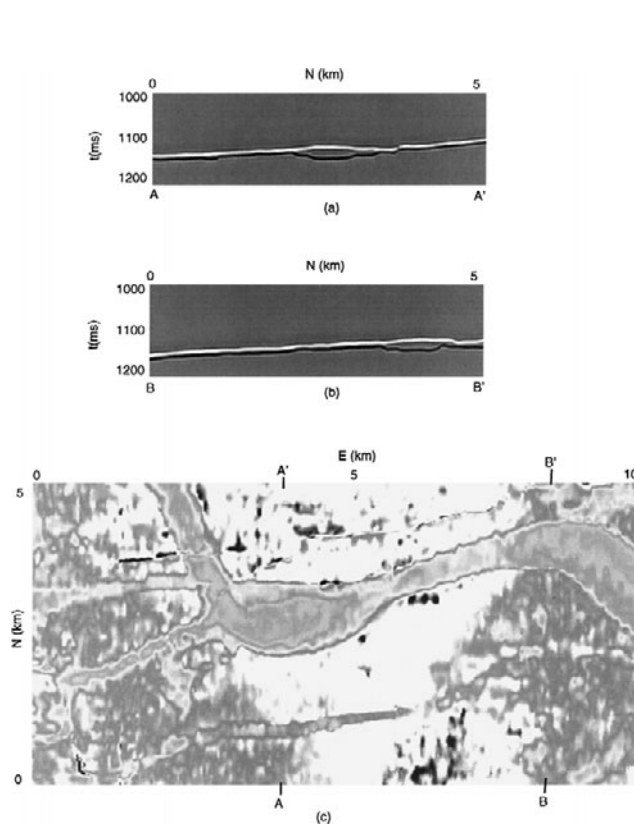


FIG. 5. (a) and (b) Cross-sections through a synthetic model derived from the picks shown in Figure 4a, where we assume $r_1/r_2 = -0.9$. (c) An amplitude extraction map of the synthetic model corresponding to the top pick.

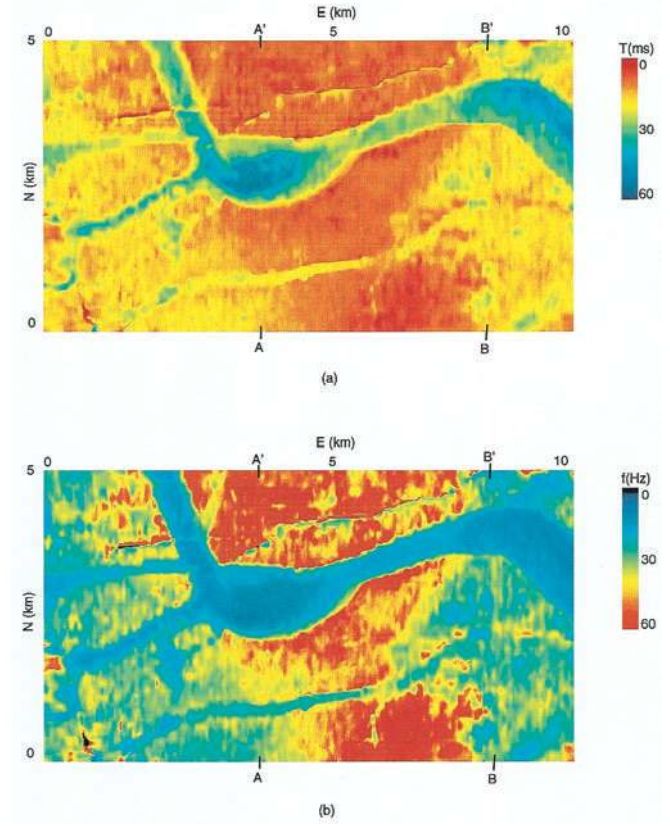


FIG. 6. (a) Normal incidence two-way traveltime thickness $T(x, y)$ corresponding to the picks shown in Figure 4a. (b) The peak frequency $f = 1/2T$ predicted by equation (2) and Figure 2b for $r_1/r_2 = -0.9$.

limits of the channel, the peak frequency shown in Figure 8a is not unlike the peak frequency shown for the synthetic in Figure 6b. Outside the channel, the results are quite different, since there was no reflector corresponding to the channel bottom. The peak amplitude $a_j(f^{\text{peak}}, t)$, shown in Figure 9a, shows considerable amplitude variation and mimicks the variation seen on the amplitude extraction in Figure 4c. The lower amplitude in the right-hand side of the picture is the result of an overlying erosional surface that has cut into our analysis window. The trough frequency $f^{\text{trough}}(t)$ shown in Figure 8b is, as expected, quite a bit noisier than the peak frequency estimate shown in Figure 8a.

Comparison to conventional attributes

In Figure 7 we display the response envelope and response frequency extracted along the horizon bounding the channel from above. While we can see the same general features in the response frequency (Figure 7b) as in the peak frequency (Figure 8a) in zones of good S/N ratio, the peak frequency has a one-to-one correlation with the theoretical tuning frequency shown in Figure 6b. The response frequency, on the other hand, is off by some spatially variable scale factor. The response frequency differs from the peak frequency defined implicitly by equation (16) in two ways. First, instantaneous frequency (from which the response frequency is derived) is a measure of the average frequency within the seismic wavelet being

analyzed (Cohen, 1993). In general, the average of a spectrum differs from its statistical mode, or peak. Second, for thicker parts of the channel where the upper and lower reflections do not significantly interfere, the response/instantaneous attributes do not see the lower reflector, although they both may fall within our 100-ms spectral decomposition analysis window. To this end we define the mean frequency and mean amplitude of our spectral analysis to be

$$a_j^{\text{mean}}(t) = \frac{1}{(K_2 - K_1 + 1)} \sum_{k=K_1}^{K_2} a_j(f_k, t) \quad (18)$$

and

$$f_j^{\text{mean}}(t) = \frac{\sum_{k=K_1}^{K_2} a_j(f_k, t) f_k}{\sum_{k=K_1}^{K_2} a_j(f_k, t)}, \quad (19)$$

and we display the results in Figures 8c and 9c. We note that $f_j^{\text{mean}}(t)$ has the same limited dynamic range ($20 \text{ Hz} < f_j^{\text{mean}} < 35 \text{ Hz}$) as the response frequency shown in Figure 7b but shows the channel along its entire length. Indeed, the mean frequency and mean amplitude show a more continuous channel image than the peak frequency and peak amplitude shown in Figures 8a and 9a. In particular, the two point-bar features indicated by arrows are clearly discernible on the mean amplitude attribute in Figure 10c. We also note the north-south acquisition footprint in Figure 9c. The amplitudes in Figure 9a were calculated by finding the maximum of the curve through the three samples clustered around the peak amplitude. The amplitudes in Figure 9c were calculated as the mean of all 26 frequencies. A more robust least-squares peak amplitude estimator that uses more than three points might provide better results.

Change of phase with frequency

We noted in Figure 3 a rapid phase change at the tuning frequencies (either notches or peaks). If we assume the phase of the incident seismic wavelet varies slowly with frequency, we should theoretically be able to use this rapid phase change as an indicator of spectral tuning on seismic horizon slices, even if we do not know the exact amplitude spectrum. Because of phase wrapping problems, we follow Taner et al.'s (1979) definition of phase change with time [equation (8)] and calculate the phase change with frequency to be

$$\begin{aligned} \frac{\partial}{\partial f} \phi_j(f, t) &= \frac{\partial}{\partial f} \tan^{-1}[v_j(f, t)/u_j(f, t)] \\ &= 2\pi \frac{u_j(f, t) \frac{\partial}{\partial f} v_j(f, t) - v_j(f, t) \frac{\partial}{\partial f} u_j(f, t)}{a_j(f, t)^2}. \end{aligned} \quad (20)$$

We display $(\partial/\partial f)\phi_j(f, t)$ in Figure 10 for the top of the channel shown in Figure 4 for $f = 25 \text{ Hz}$ and $f = 55 \text{ Hz}$. After considerable testing, we conclude that our numerical derivatives in calculating $\partial u/\partial f$ and $\partial v/\partial f$ in equation (21) are overly

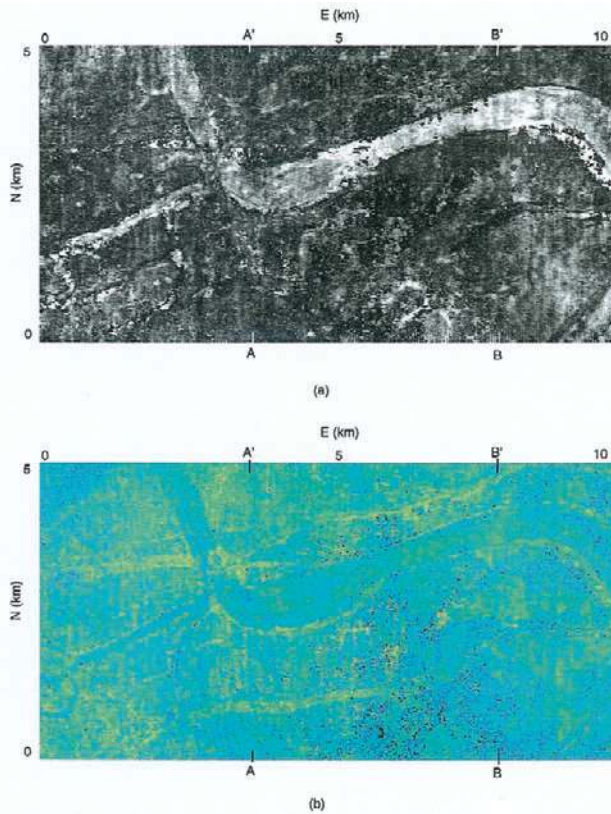


FIG. 7. The (a) response envelope and (b) response frequency corresponding to the top of the channel shown in Figure 5. Both attributes are sensitive to channel thickness. Color scale is the same as in Figure 6b.

sensitive to noise, such that $\partial\phi/\partial f$, like f^{trough} , is a poor attribute for thin-bed analysis.

Application to the paleo-Mississippi River, offshore Gulf of Mexico

We now apply our new attributes to a large spec data set collected by Geco-Prakla in the Gulf of Mexico. This same data

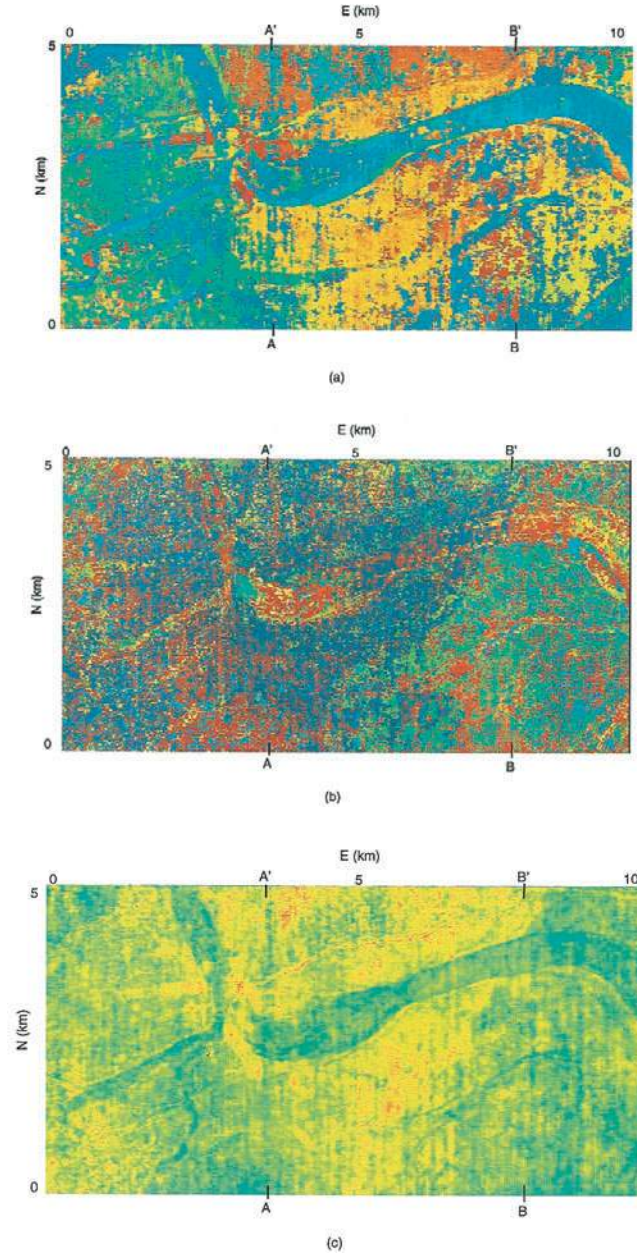


FIG. 8. The (a) peak frequency $f^{\text{peak}}(t)$, (b) trough frequency $f^{\text{trough}}(t)$, and (c) mean frequency $f^{\text{mean}}(t)$ corresponding to the top of the channel shown in Figure 4. We calculated 35 frequencies ranging between 10 and 70 Hz at a 2-Hz increment within a 100-ms analysis window. The mean frequency looks quite similar to the response frequency in Figure 7b as predicted by Cohen (1993). Color scale is the same as in Figure 6b. Green at the deepest point of the channel in (a) corresponds to the second peak shown in Figure 2a, since the first peak falls below the seismic band.

set was analyzed by Marfurt et al. (1998) and Gersztenkorn and Marfurt (1999) for coherence, by Partyka et al. (1999) for spectral decomposition, and by Marfurt and Kirlin (2000) for amplitude gradients. The geologic setting is summarized by Haskell et al. (1998) to be that of mostly sand-filled channels in a shale matrix corresponding to the Mississippi River delta during Pleistocene age.

We reproduce the C3 coherence image produced by Gersztenkorn and Marfurt (1999) in Figure 11. Seismic coherence allows us to easily recognize the main trunk of the paleo-Mississippi River at the north end of the survey. This trunk bifurcates into a number of large distributary channels, much as seen in the modern Mississippi bird-foot delta complex. The

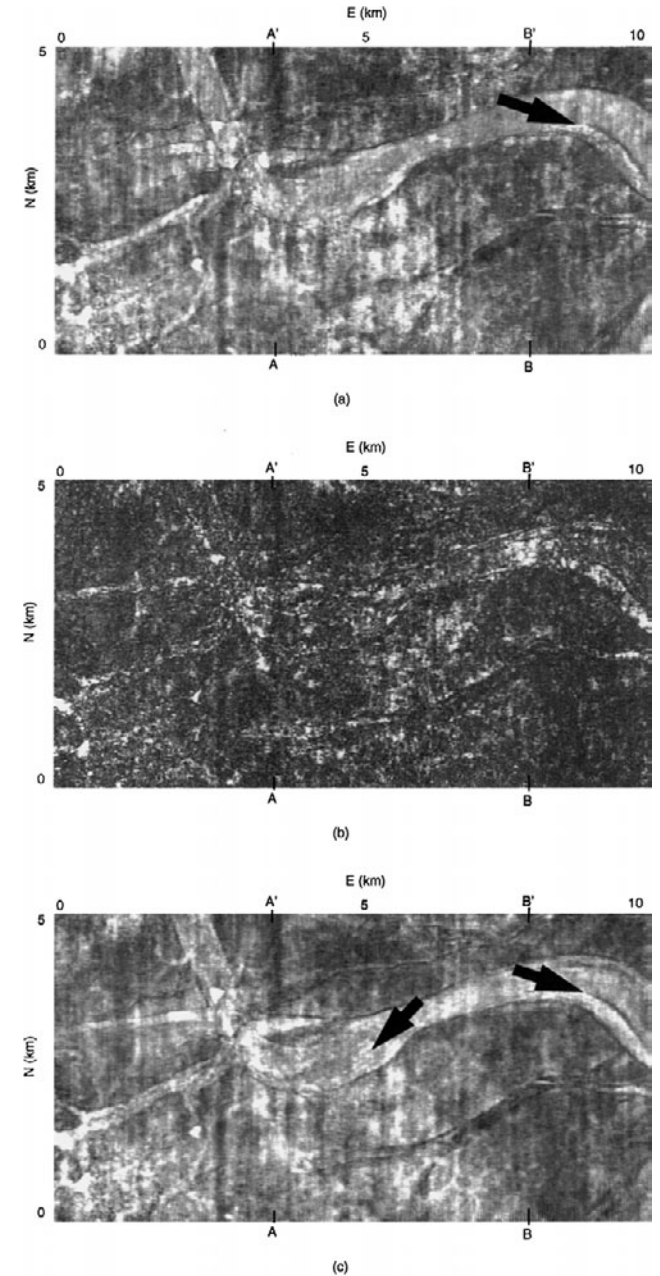


FIG. 9. (a) Maximum amplitude $a^{\text{peak}}(t)$, (b) minimum amplitude $a^{\text{trough}}(t)$, and (c) mean amplitude of the data in Figure 4.

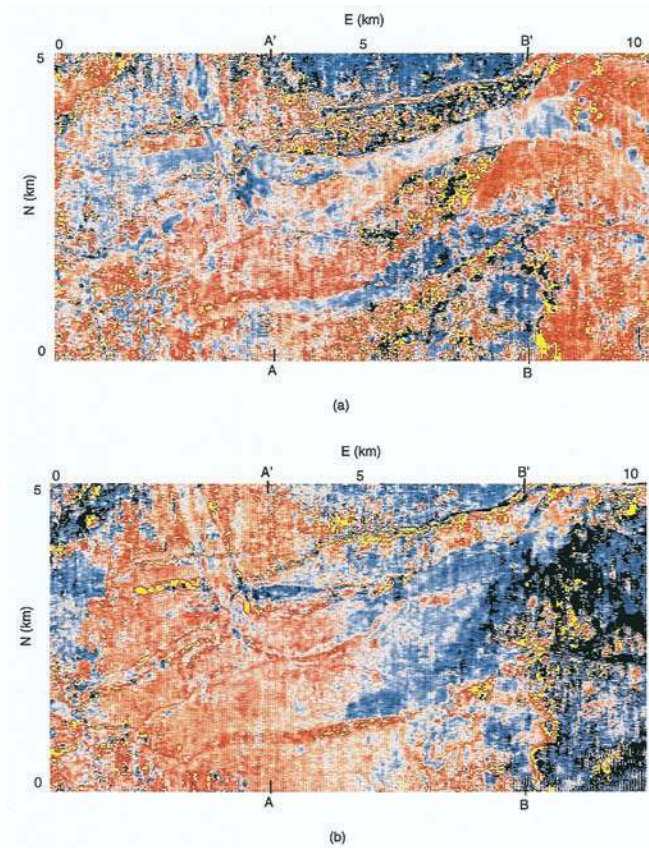


FIG. 10. Phase change with frequency $\partial\phi(f, t)/\partial f$ evaluated along the top of the channel shown in Figure 5 at (a) 25 Hz and (b) 55 Hz.

seismic horizon was obtained by manually picking an easily recognizable peak along every ten lines in the north-south and east-west directions and then interpolating the picks. Because of faulting and other wavelet changes, we recognize some very obvious errors in our picking. We leave these busts in our horizon extraction to underscore that this kind of attribute analysis is commonly done very early in the evaluation of acreage, providing us a quick look at the major structural and stratigraphic features in the data before conventional interpretation at the prospect level begins. We note the small fault-controlled channel feature indicated by the box that we extracted and displayed in Figure 4. (For the calibration effort carried out using the data in Figure 4, we carefully repicked the top of the channel as the appropriate peak-to-trough zero crossing rather than as a simple peak. We also picked the bottom of the channel for generating our synthetic in Figure 5 to be a trough-to-peak zero crossing. This allowed us to approach zero thickness away from the channel.)

We perform a spectral analysis between 10 and 70 Hz using a 2-Hz increment in a 100-ms window and display the peak frequency, f^{peak} , in Figure 12. To more easily interpret the thickness variation within the distributary-channel features, we merge the coherence in Figure 11 with the peak frequency in Figure 12 and generate a composite multiattribute image in Figure 13 by interleaving adjacent pixels. The interleaving of high-coherence white with the peak-frequency color map renders an image that is somewhat more pastel than we would desire, but improvement of multiattribute display software is beyond the immediate scope of this paper. Zones of low coherence show up as dark zones on our multiattribute display. This multiattribute display aids us in two ways: (1) it delineates edges between distinct lithologic or structural units and (2) it focuses our attention on the high-coherence events internal to

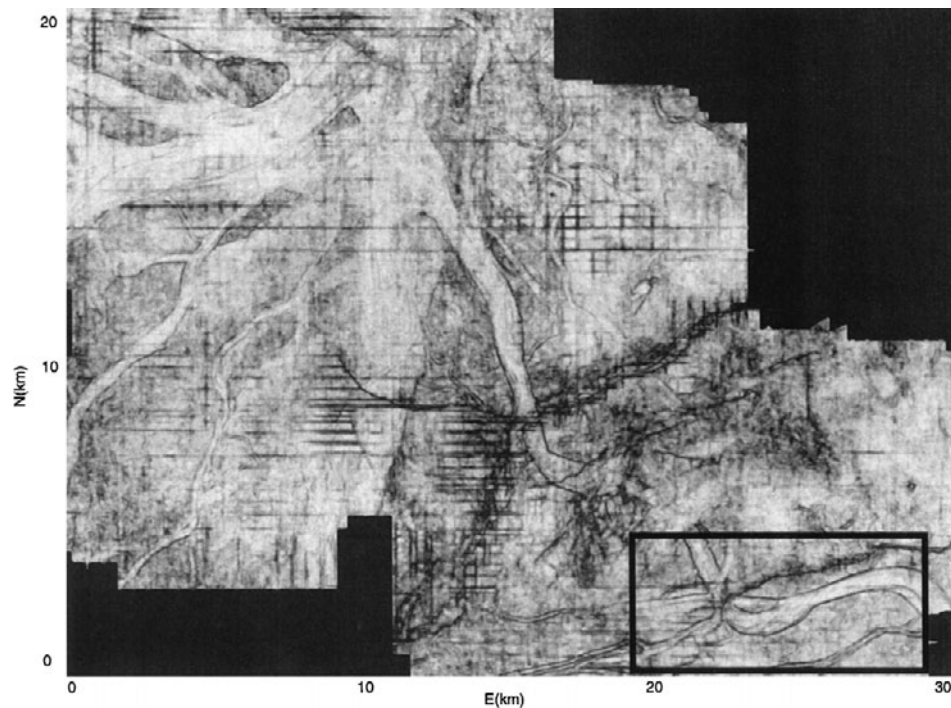


FIG. 11. Eigenstructure, or C3 coherence, calculated along an interpreted Pleistocene horizon showing the paleo-Mississippi distributary-channel system.

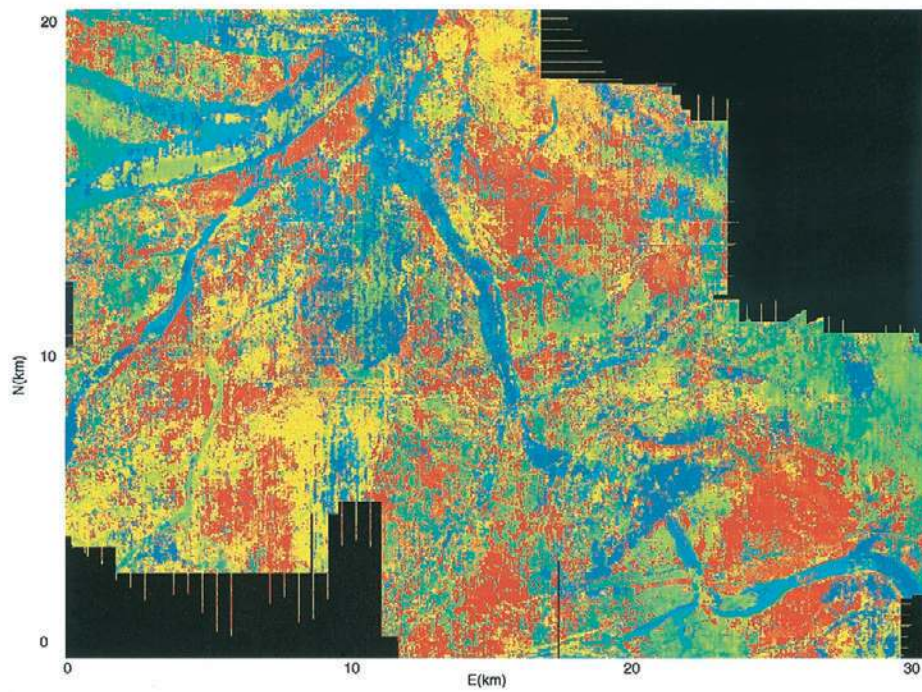


FIG. 12. Peak frequency f^{peak} calculated over a 100-ms window centered about the same horizon used in Figure 11.

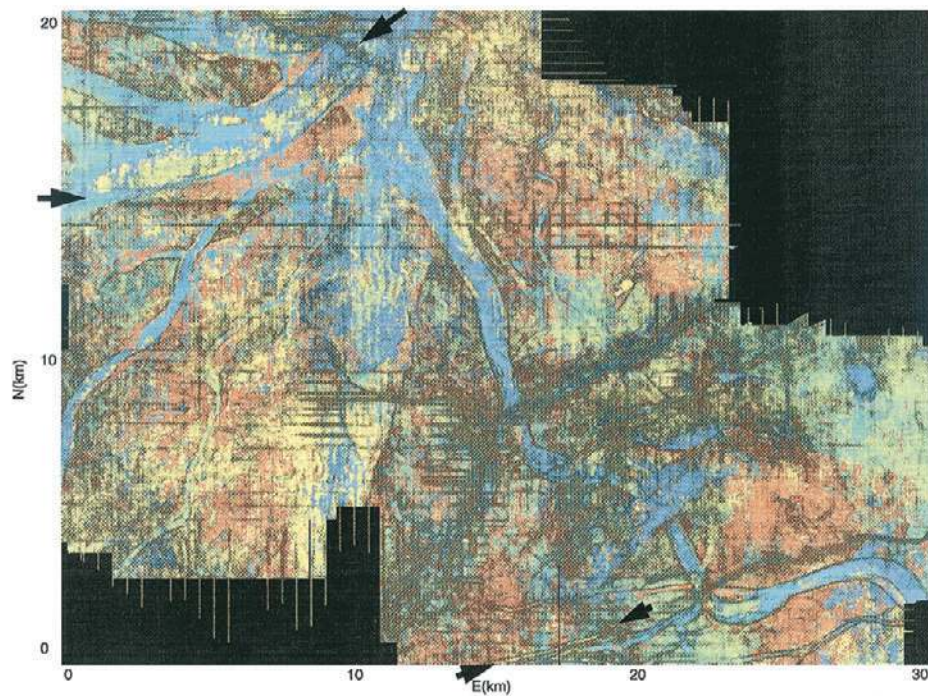


FIG. 13. A simple multiattribute display generated by interleaving the peak frequency displayed in Figure 12 with the coherence displayed in Figure 11 that allows us to focus on thin-bed tuning within the distributary system. The wider, deeper portions of the trunk have a low peak frequency and are displayed in blue. The narrower, shallower distributary channels have a higher peak frequency and are displayed in cyan, green, and yellow such as the channel indicated by arrows in the southeastern part of the image. The anomalous (high green peak frequency) features indicated by arrows in the northwestern part of the image in the channel centers correspond to the second peak shown in Figure 2a, since the first peak falls below the seismic band.

the channel boundaries and away from the low-coherence (and often low S/N ratio) events elsewhere.

The wider/thicker trunk and tributary channels are displayed in shades of blue, corresponding to a low tuning frequency. The narrower (and shallower) channels further toward the sea are displayed in shades of cyan and green, corresponding to a moderate tuning frequency. The narrowest (and presumably thinnest) channels are displayed in shades of yellow, corresponding to a tuning frequency falling within the upper third of our analysis spectrum. We note in particular a green channel that trifurcates into three narrower yellow channels toward the bottom of our image. The point bar discussed in Figure 5c also produces a change in channel depth and is displayed as green within a channel that is otherwise cyan or blue.

The quick interpretation of this seismic horizon took a full day on a modern interpretive workstation. Calculating the spectral attributes about this horizon took <1 hour on a Sparc 20 computer. Calculating the peak frequency and peak amplitude took slightly more than 24 hours for the entire cube of data containing 1500 times samples on the same hardware. The image shown in Figure 13 does not provide the same ability to quantitatively predict metric thickness and porosity that could possibly be obtained using inversion for acoustic impedance. Nevertheless, if we understand the depositional system and have a solid foundation in sedimentology and sequence stratigraphy, the combined multiattribute image shown in Figure 13 allows us to quickly generate prospects for more careful study.

CONCLUSIONS

We have developed a suite of new single- and multitrace attributes based on spectral analysis of seismic reflectivity to better map internal changes within thin-bed reservoirs. Some of these attributes, such as the amplitude and frequency of the spectral notches as well as the change of phase with frequency, behave very poorly in the presence of noise. In contrast, the amplitude and frequency of the spectral peak can be quite useful in quantifying thickness in thin-bed reservoirs such as a sand channel embedded in a shale matrix. Through synthetics, we have shown that the peak frequency is more quantitatively connected to the expected tuning frequency than the commonly used instantaneous or response frequency attributes. We feel that careful poststack seismic inversion for acoustic impedance will almost always be superior to any thin-bed attribute derived in this paper. Unfortunately, we often lack the well control necessary to generate an accurate a priori estimate of the background seismic impedance model and seismic source wavelet required for impedance inversion. Even when we have such well control, a careful background model may take weeks or months to generate.

Finally, the peak frequency and peak spectral amplitude attributes described here allows us to reduce the 20–50 components generated by spectral decomposition to two attributes that define the essence of the reflectivity spectrum. This allows us to analyze large 3-D seismic data sets using conventional interpretation hardware as well as more advanced multiattribute tools such as geostatistics, neural nets, and feature analysis.

ACKNOWLEDGMENTS

The original observation of the value of peak frequency was made by Kurt Toellestrup and Charlie Mims of Amoco's Offshore Business Unit in 1995, working with the original spectral decomposition cube developed by Greg Partyka and James Gridley. We are grateful to them and to the entire Amoco Enhanced Multiattribute Seismic Analysis (EMSA) team. Special thanks to Susan Nissen for her interpretation of the channel sands displayed in Figure 4 and to Vicki Wilson and Linda Massey of Amoco's ATTC document services group for their care in preparing this document.

REFERENCES

- Bahorich, M. S., and Bridges, S. R., 1992, The seismic sequence attribute map (SSAM): 42nd Ann. Internat. Mtg., Soc. Expl. Geophys., Expanded Abstracts, 227–230.
- Bahorich, M. S., and Farmer, S. L., 1995, 3-D seismic discontinuity for faults and stratigraphic features: The coherence cube: *The Leading Edge*, **14**, 1053–1058.
- Bodine, J. H., 1986, Waveform analysis with seismic attributes: *Oil & Gas J.*, **84**, June, 59–63.
- Cohen, L., 1993, Instantaneous 'anything': *Proc. IEEE Conf. Acoust. Speech Signal Proc.*, **4**, 105–109.
- Dalley, R. M., Gevers, E. E. A., Stampfli, G. M., Davies, D. J., Gastaldi, C. N., Ruijtenberg, P. R., and Vermeer, G. J. D., 1989, Dip and azimuth displays for 3-D seismic interpretation: *First Break*, **7**, 86–95.
- Gersztenkorn, A., and Marfurt, K. J., 1999, Eigenstructure-based coherence computations as an aid to 3-D structural and stratigraphic mapping: *Geophysics*, **64**, 1468–1479.
- Haskell, N. L., Nissen, S. F., Lopez, J. A., and Bahorich, M. S., 1998, 3-D seismic coherency and the imaging of sedimentological features in predictive high resolution sequence stratigraphy, in Gradstein, F. M., Sandvik, K. O., and Milton, N. J., Eds., *Sequence stratigraphy concepts and applications*: Elsevier Science Publ. Co., Inc., 197–214.
- Hesthammer, J., 1998, Evaluation of the timedip, correlation and coherence maps for structural interpretation of seismic data: *First Break*, **16**, 151–165.
- Hesthammer, J., and Fossen, H., 1997, Seismic attribute analysis in structural interpretation of the Gullfaks field, northern North Sea: *Petrol. Geosci.*, **3**, 13–26.
- Kelley, M. C., Lindsay, R. O., and Clawson, S. R., 1992, A method of geophysical exploration: United States Patent 5 136 552.
- Luo, L., Higgs, W. G., and Kowalik, W. S., 1996, Edge detection and stratigraphic analysis using 3-D seismic data: 66th Ann. Internat. Mtg., Soc. Expl. Geophys., Expanded Abstracts, 324–327.
- Marfurt, K. J., and Kirlin, R. L., 2000, 3-D broad-band estimates of reflector dip and amplitude: *Geophysics*, **65**, 304–320.
- Marfurt, K. J., Kirlin, R. L., Farmer, S. H., and Bahorich, M. S., 1998, 3-D seismic attributes using a running window semblance-based algorithm: *Geophysics*, **63**, 1150–1165.
- Neidell, N. S., and Poggiagliomi, E., 1977, Stratigraphic modeling and interpretation—Geophysical principles and techniques, in Peyton, C. E., Ed., *Seismic stratigraphy applications to hydrocarbon exploration*: AAPG Memoir **26**, 389–416.
- Okaya, D. A., 1995, Spectral properties of the earth's contribution to seismic resolution: *Geophysics*, **60**, 244–251.
- Partyka, G. A., Gridley, J. A., and Lopez, J. A., 1999, Interpretational aspects of spectral decomposition in reservoir characterization: *The Leading Edge*, **18**, 353–360.
- Peyton, L., Bottjer, R., and Partyka, G. A., 1998, Interpretation of incised valleys using new 3-D seismic techniques: A case history using spectral decomposition and coherency: *The Leading Edge*, **17**, 1294–1298.
- Radovich, B. J., and Oliveros, R. B., 1998, 3-D sequence interpretation of seismic instantaneous attributes from the Gorgon field: *The Leading Edge*, **17**, 1286–1293.
- Robertson, J. D., and Nogami, H. H., 1984, Complex seismic trace analysis of thin beds: *Geophysics*, **49**, 344–352.
- Taner, M. T., Koehler, F., and Sheriff, R. E., 1979, Complex seismic trace analysis: *Geophysics*, **44**, 1041–1063.
- Widess, 1973, How thin is a thin bed: *Geophysics*, **38**, 1176–1180.